Supplementary Information

The size-dependent valence and conduction band-edge energies of Cu quantum dots

Takahiro Matsui,[a] Hiroto Watanabe,[a*] Shoichi Somekawa,[b] Sayaka Yanagida,[b] Yuya Oaki,[a] and Hiroaki Imai[a*]

[a] Department of Applied Chemistry, Faculty of Science and Technology, Keio University, 3-14-1 Hiyoshi, Kohoku-ku, Yokohama 223-8522, Japan.
E-mail: hiroaki@applc.keio.ac.jp
[b] Tokyo Metropolitan Industrial Technology Research Institute, 2-4-10 Aomi. Koto-ku, Tokyo 135-0064, Japan.

Table of contents

Supplementary Information section 5: Determination of the valence state of CuO QDs and Cu QDs by X-ray absorption near-edge structure measurements.

Supplementary Information section 6: Determination of the band structure of CuO QDs and Cu QDs

Supplementary Information section 7: Curve fitting with effective mass approximation (EMA) for CuO QDs and Cu QDs

Supplementary Information section 1: Experimental Information

Materials

Tetraethyl orthosilicate (TEOS) as a silica source and hexyltrimethylammonium bromide (C6TAB), trimethyltetradecylammonium chloride (C12TAC), and trimethylstearylammonium chloride (C18TAC) as templates for porous silica were purchased from Tokyo Chemical Industry. Copper(II) nitrate trihydrate ($Cu(NO_3)_2 \cdot 3H_2O$) and sodium tetrahydroborate ($NaBH_4$) were purchased from FUJIFILM Wako Pure Chemical. SBA-15 mesoporous silica (average pore diameter 8 nm) was purchased from Sigma-Aldrich. All the materials were used as purchased.

Supplementary Information section 2: Preparation and characterization of porous silicas

Solvent-free synthesis of porous silicas (PSs)

Alkyltrimethylammonium chloride (bromide) (CnTAC(B)), (n = 6–18; n: carbon number of the alkyl chain), tetraethyl orthosilicate (TEOS), and pH 2.0 HCl aq. were mixed at a 0.2:1.0:4.0 mole ratio, respectively. After stirring the mixture at 298 K until gelation, the products were dried at 333 K for 24 h and calcined at 873 K for 3 h to obtain PSs. The detailed synthesis procedures and the characterization of SMPS can be found in our previous report.[1]

Characterization of porous silicas

The nitrogen adsorption–desorption isotherms were obtained at 77 K with 3Flex-3MP (Micromeritics) using samples pretreated under vacuum at 433 K for 5 h. The specific surface area was calculated using the Brunauer–Emmett–Teller (BET) method. The pore-size distribution was calculated using the Barrett–Joyner–Halenda (BJH) method and the Grand Canonical Monte Carlo (GCMC) method. For the GCMC method, BEL-Master™ software Ver. 6.4.10 (Nihon BEL, Inc.) was used for analysis, assuming an oxygen-exposed surface with a cylindrical pore structure; adsorbate: nitrogen; peak assumption: Gaussian model with a single peak.

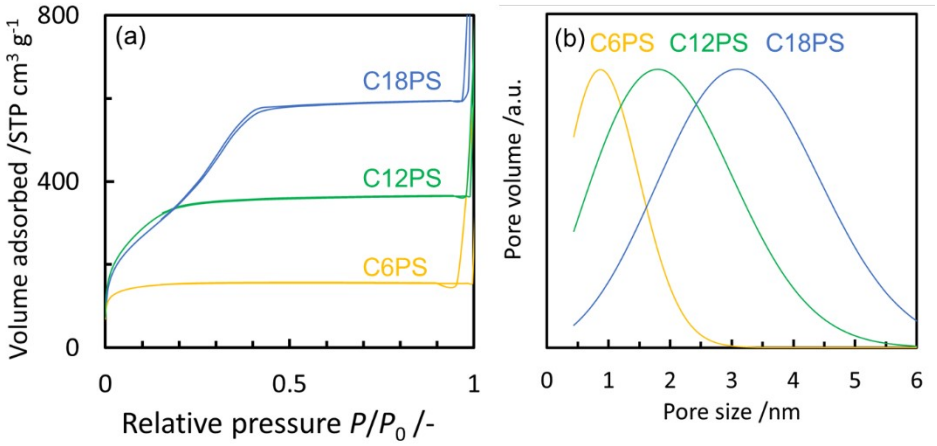

Figure S1 (a) Nitrogen adsorption–desorption isotherms and (b) the GCMC pore-size distribution of porous silicas synthesized with various surfactants: C18TAC (blue), C12TAC (green), and C6TAC (yellow).

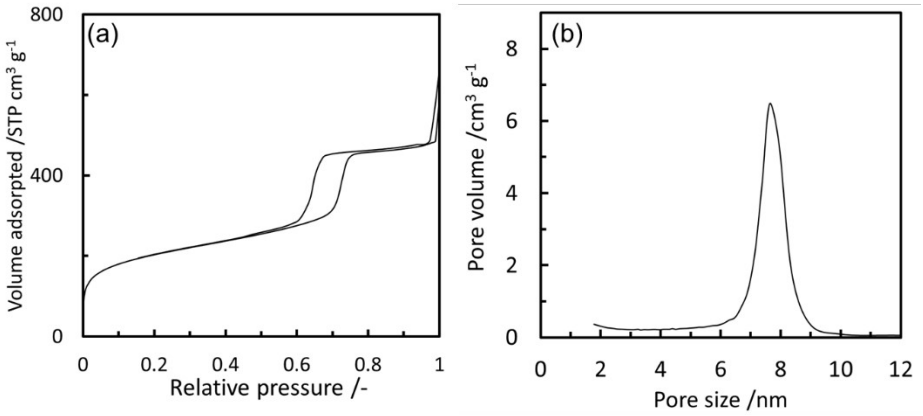

Figure S2 (a) Nitrogen adsorption–desorption isotherms and (b) the BJH pore-size distribution of SBA-15.

Table S1. Textual properties of porous silicas

sample	Specific surface area[(a)] (m^2/g)	pore volume[(a)] (cm^3/g)	pore size (nm)
C6PS	540	0.24	0.87[(b)]
C12PS	1203	0.56	1.82[(b)]
C18PS	1556	0.85	3.04[(b)]
SBA-15	694	0.75	7.63[(c)]

(a) Calculated using the BET method. (b) Calculated using the GCMC method. (c) Calculated using the BJH method.

Supplementary Information section 3: Preparation of CuO QDs and Cu QDs

Preparation of CuO QDs in PSs

CuO QDs were prepared in porous silicas, using a $Cu(NO_3)_2$ aqueous solution as a precursor. A powder of PSs was dried under vacuum in a round-bottomed flask equipped with a magnetic stirring bar before impregnation. A certain concentration of $Cu(NO_3)_2$ (0.05–5 mol/dm^3) aqueous solution was injected into the PSs, and the precursor solution was introduced into the pores of PSs with vigorous mixing. The volume of impregnated precursor solution was fixed to equal the pore volume of the PSs. After complete impregnation, the power was dried under vacuum for 5 h. A dried powder was calcined at 873 K in air for 3 h to obtain CuO QDs in the pores of PSs.

Preparation of Cu QDs in PSs

Cu QDs were prepared by introducing a reductant solution into the pores of PSs containing CuO QDs. For the preparation of reductant solutions, a powder of $NaBH_4$ was dissolved into ethanol (1 mol/dm^3) or a 1 mol/dm^3 NaOH aqueous solution (5 mol/dm^3). 1 mol/dm^3 ethanolic solution was used for the reduction of CuO QDs produced with a $Cu(NO_3)_2$ concentration below 1 mol/dm^3, and 5 mol/dm^3 basic aqueous solution was used for a concentration above 1 mol/dm^3. A powder of PSs containing CuO QDs was dried under vacuum in a round-bottomed flask equipped with a magnetic stirring bar before impregnation with the reductant solution. A reductant solution was injected into the PSs, and the powder was vigorously mixed until the entire solution was introduced into the pores of PSs. The volume of the injected precursor solution was fixed to equal the pore volume of PSs to avoid the undesired outflow of Cu QDs from the pores. After complete impregnation, the as-prepared powder was immediately transferred to the sample cell for the spectroscopic measurements. The spectroscopic experiments with Cu QDs were conducted with samples containing the reductant solution inside the pores of PSs to avoid aerobic oxidation of Cu QDs.

Supplementary Information section 4: Particle size analysis of CuO QDs and Cu QDs

Particle size analysis of CuO QDs and Cu QDs via TEM observation

The sizes of the CuO QDs and Cu QDs were characterized using a transmission electron microscope (TEM, FEI Tecnai G2-F20).

For the CuO QD observation, a powder of PSs containing CuO QDs was vigorously milled with an agate mortar and pestle to produce small flakes of PSs with a diameter under 100 nm. The obtained fine powder was dispersed in water, and the suspension was ultrasonicated for 5 min. Five microliters of the suspension was dropped onto a TEM grid (200-mesh Cu grid with carbon networks of 3–4 mm open pores, Nissin EM Co., Ltd.) pre-heated on a hot-plate to 393 K. The suspension droplet was dried by continuous heating at 393 K. This process was repeated twice. Finally, the grid was dried under vacuum for 5 h before TEM observation. The average diameter and the distribution were analyzed by curve fitting of the particle size distribution profiles by using the Origin Pro software with gaussian distribution.

For the Cu QD observation, the TEM grid containing a CuO QD sample prepared according to the above procedure was soaked to the reductant solution for 5 sec. After that, the grid was soaked in ethanol to remove the excess reductant solution. The surface of the grid was dried by blotting it between two filter papers several times and immediately transferred into a vacuum chamber of TEM.

Especially for Cu QDs, aggregation and growth of the particles occurred during the high magnitude TEM observations (Figure S5). Furthermore, the aggregation and growth also occurred during reduction process mainly outside of the pores (Figure S6). Therefore, the particle size distribution profiles shown in Figure S4 have multimodal characters. However, their contribution to the spectral observations is less significant due to their small amounts. We analyzed the particle size distribution profiles by deconvoluting the distribution of the primally and the aggregated particles by using the Origin Pro software with gaussian distribution and determine the average size and dispersity of the primally particles from TEM images.

The sizes of the CuO and Cu QDs were summarized in Table S2.

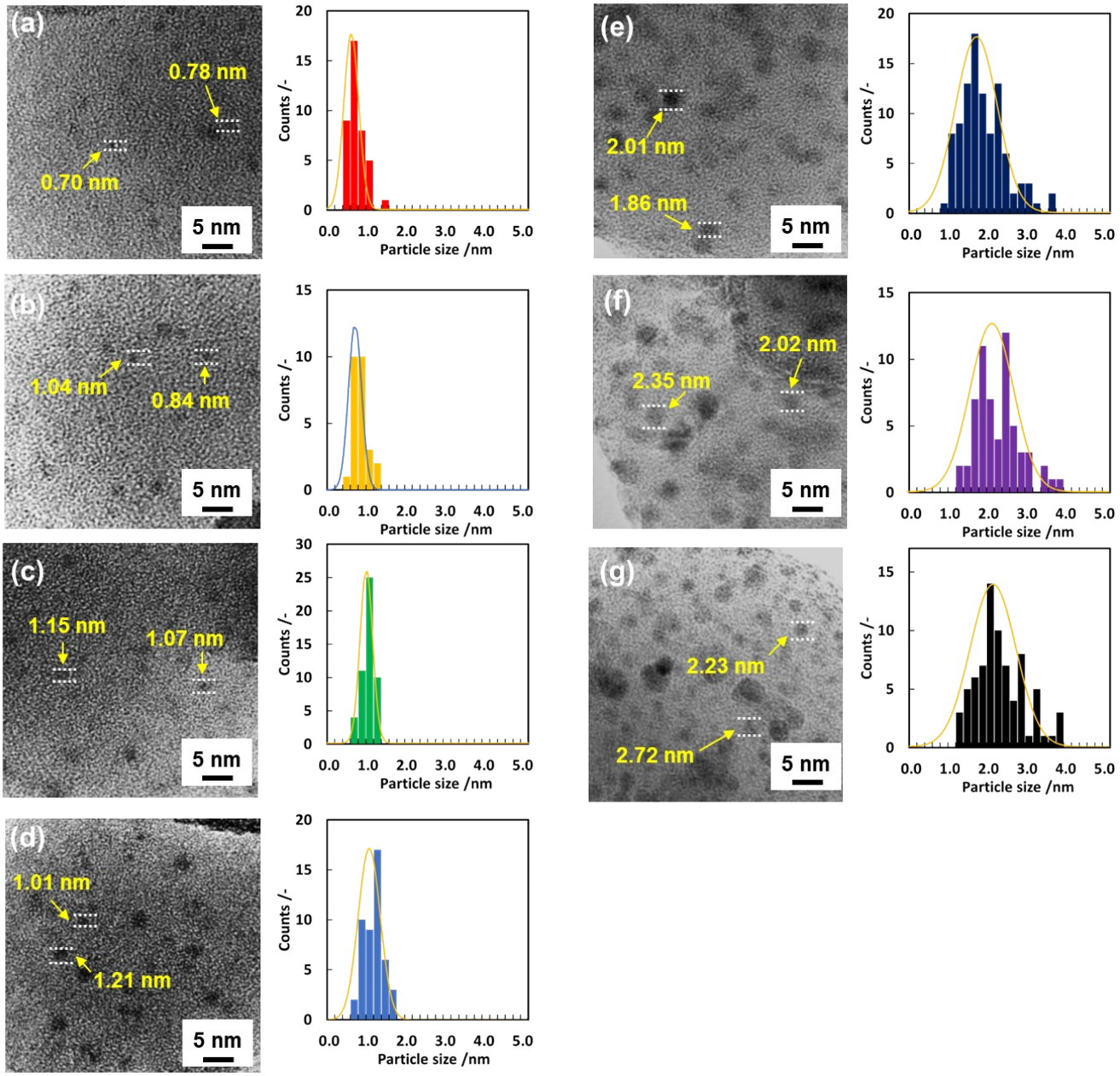

Figure S3 TEM images and particle-size distribution of CuO QDs. (a) C6-0.05M, (b) C6-0.2M, (c) C12-0.2M, (d) C18-0.2M, (e) C18-1M, (f) C18-5M, (g) SBA15-5M. The fitting curves are represented with solid lines.

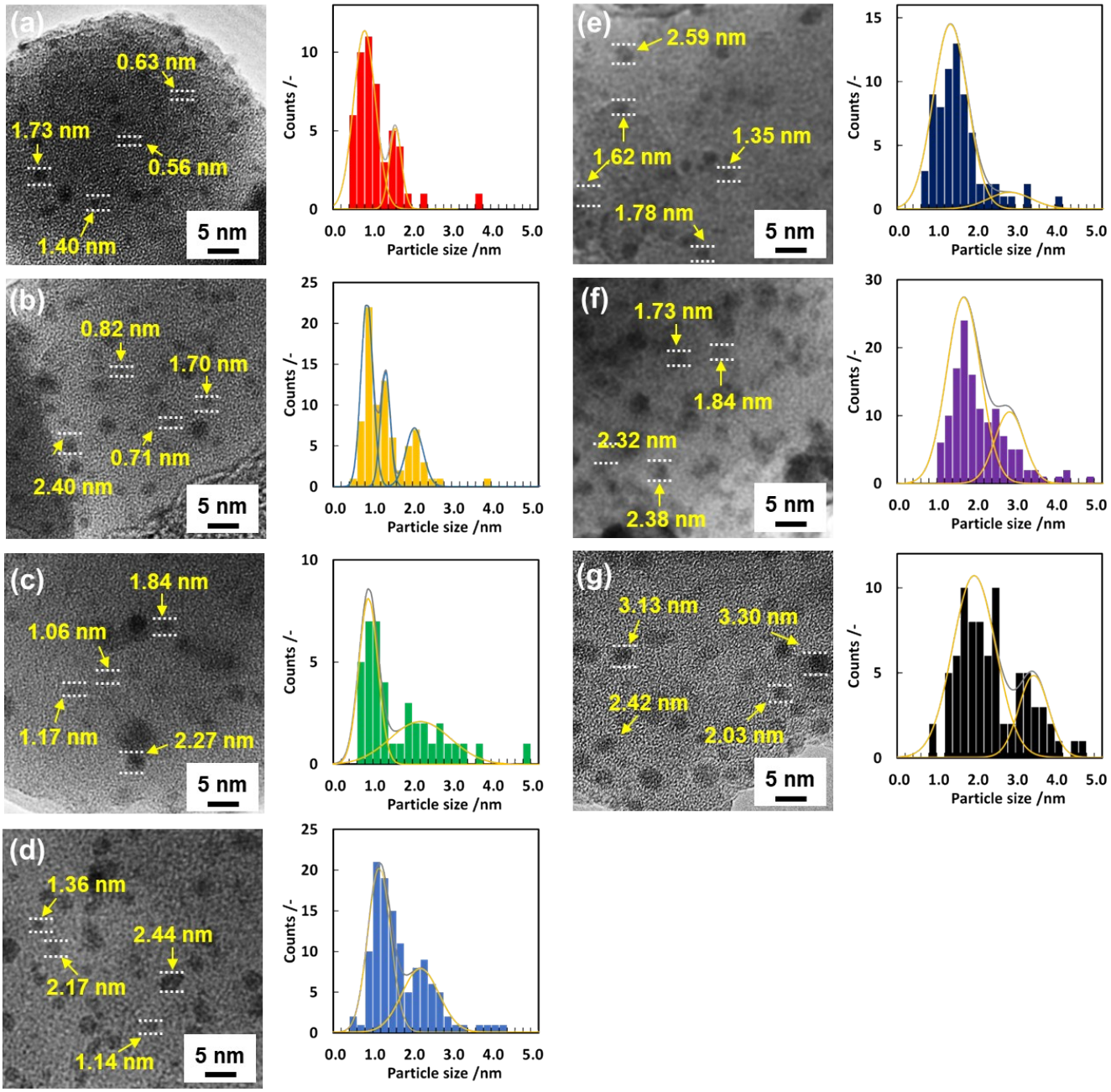

Figure S4 TEM images and particle-size distribution of Cu QDs. (a) C6-0.05M, (b) C6-0.2M, (c) C12-0.2M, (d) C18-0.2M, (e) C18-1M, (f) C18-5M, (g) SBA15-5M. The fitting curves are represented with solid lines.

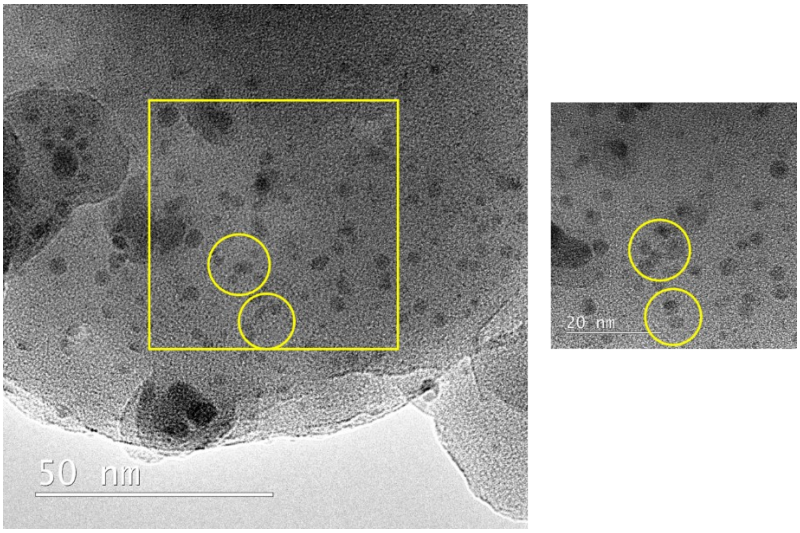

Figure S5 TEM images of Cu QDs damaged during observation. (Left) Low-magnification image. (Right) High-magnification image taken after the low-magnification observation. The small particles drifted and merged to form larger particles during exposure to the electron beam.

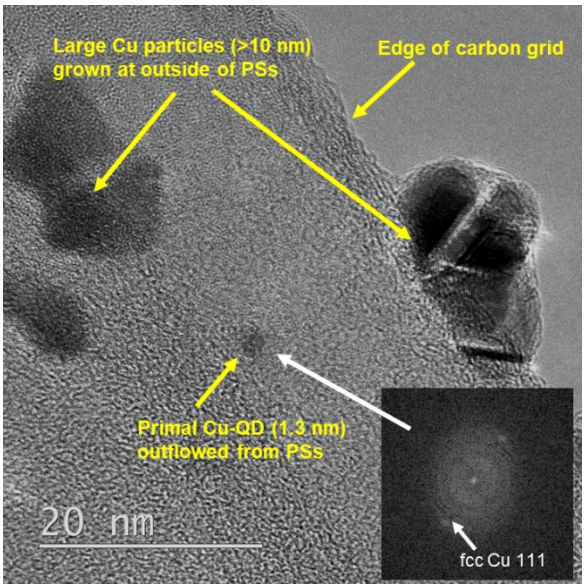

Figure S6 TEM image of Cu QDs that flowed from the pores of PSs and large Cu particles formed during the reduction process (C18-0.2M). The image was taken at the edge of the carbon grid.

Table S2 The size of CuO and Cu QDs measured from TEM images

Sample name	Synthesis condition		Average particle diameter[a]			
	Porous silica	Precursor concentration (mol/dm^3)	CuO QDs (nm)	Cu QDs (nm)	Amounts of Cu/SiO_2[b] ($\mu mol/g$)	Estimated number of Cu atoms per a particle[c]
C6-0.05M	C6PS	0.05	0.61	0.75	12	19
C6-0.2M	C6PS	0.2	0.71	0.80	48	23
C12-0.2M	C12PS	0.2	0.99	0.87	112	29
C18-0.2M	C18PS	0.2	1.11	1.13	170	64
C18-1M	C18PS	1.0	1.69	1.28	850	97
C18-5M	C18PS	5.0	2.10	1.61	4250	230
SBA15-5M	SBA-15	5.0	2.12	2.05	3750	383

(a) The average diameter observed from TEM images. (b) Calculated from the introduced amounts of CuO and Cu precursor to the PSs. (c) Calculated from the average diameter of Cu QDs.

Supplementary Information section 5: Determination of the valence state of CuO QDs and Cu QDs by X-ray absorption near-edge structure measurements.

The valence states of QDs before and after $NaBH_4$ reduction were measured using an X-ray absorption near-edge structure (XANES at the Aichi Synchrotron Radiation Center). We measured the Cu K-edge of the pelletized samples by transmission mode, and the measurement time was set to 60 sec. Note that the longer (over 5 min) exposure to the high-intensity X-ray causes a reduction of CuO QDs to Cu QDs; therefore, a short measurement time was used for the present study. The absorption-edge energies of CuO QDs and Cu QDs were slightly higher (~2 eV) than those of the bulk reference samples. These energy differences are probably due to the E_{cb} shift with the quantum size effect. The shoulder of the Cu K-edge absorption is attributed to the 1s to 4p transition. Because of the conduction-band edge of CuO and Cu mainly formed with Cu 4p orbitals, it is reasonable to deduce that the energy shifts due to the quantum size effect are observable with XANES spectra.

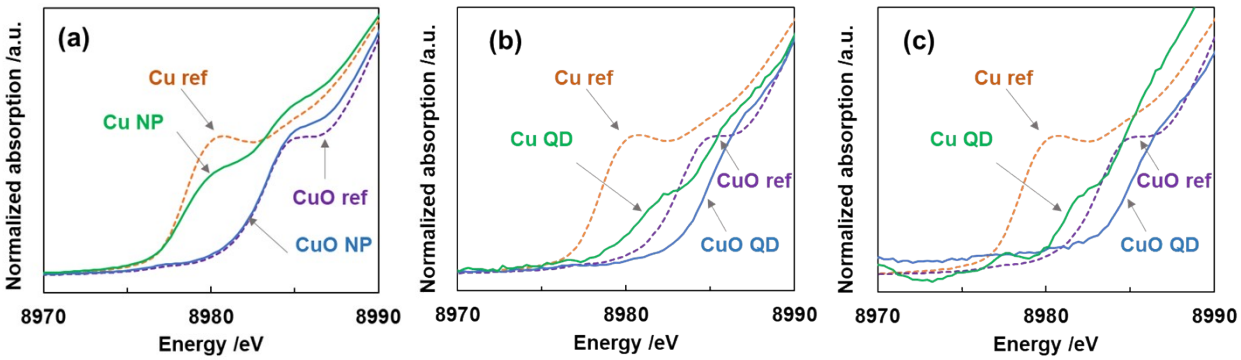

Figure S7 XANES spectra of CuO QDs and Cu QDs. (a) SBA15-5M, (b) C6-0.2 M, (c) C6-0.05M.

Supplementary Information section 6: Determination of the band structure of CuO QDs and Cu QDs

The conduction- and valence-band levels were calculated using following equations.

$$E_{vb} = -4.44 + IP$$
$$E_{cb} = E_{vb} - E_g$$

where E_g (eV) is the bandgap energy determined from UV-vis spectra, *IP* (eV) is the ionization energy with respect to the vacuum level (0 eV) determined from PYSA, E_{vb} (V_{SHE}) is the valence band–edge energy in the standard hydrogen electrode scale (SHE; 0 V_{SHE} corresponds to 4.44 eV vs vacuum level), and E_{cb} (V_{SHE}) is the conduction band–edge energy.

Determination of bandgap energies of CuO QDs and Cu QDs

The bandgap energies of CuO QDs and Cu QDs were determined from the absorption edge monitored by diffuse reflectance ultraviolet-visible (DR-UV-vis) spectra (JASCO V-670 equipped with an integral sphere).

The photon energy dependence of the absorption coefficient near the bandgap edge is described as

$$\alpha h\nu^{1/n} = k(h\nu - E_g)$$

where α is the absorption coefficient, $h\nu$ is the photon energy, E_g is the bandgap energy, *k* is the proportional factor, *n* = 2 for the allowed indirect, and *n* = 1/2 for the allowed direct transition.[2] The plots of $\alpha h\nu^{1/n}$ against $h\nu$ (Tauc plots[2]) have a linear correlation at the absorption edges, and the extrapolation of the straight line to the *x*-intercept gives the bandgap energies. Since CuO has an indirect gap, we used *n* = 2 for CuO QDs.

For Cu QDs we used n = 1/2 (direct-gap). There are two reasons. First, as described in the ref. 20, the bottom of the lowest unoccupied electronic state above the Fermi level is located at Γ point. Thus, the when the bandgap was formed with quantum-size effect, Cu expected to be turn to direct-gap semiconductor like state. Second, it is well known that the Cu QDs show fluorescence when their surface was passivated with thiol compounds. The appearance of the fluorescence is another evidence for the direct-gap character Cu QDs. We also calculated bandgaps of Cu QDs by using n = 2 and compared the results with n = 1/2 (Figure S15). A good correlation between the particle size and the bandgap was obtained only for the n = 1/2.

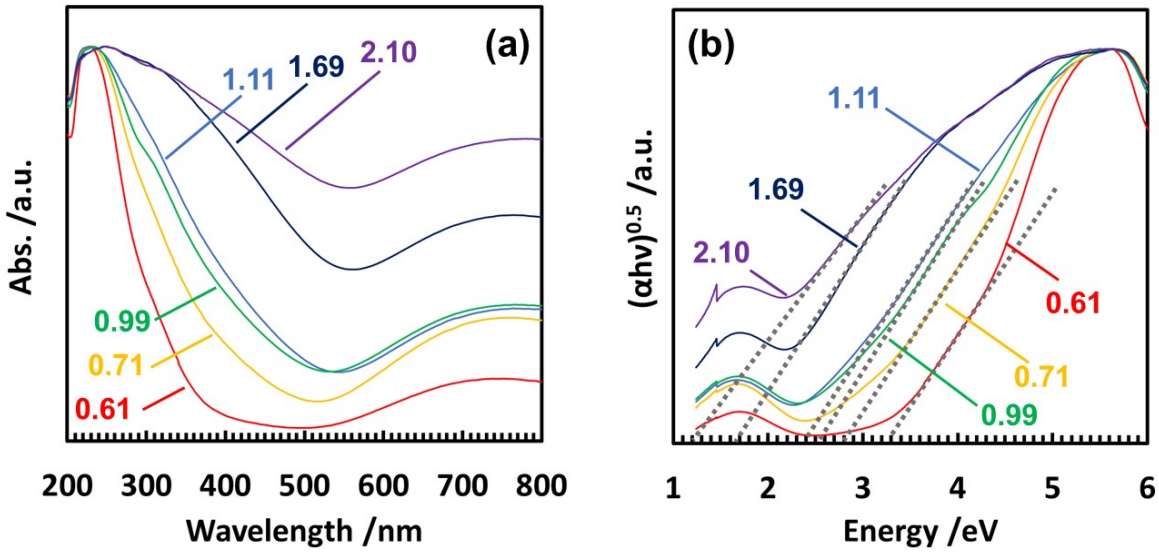

Figure S8 (a) UV-vis spectra and (b) Tauc plots of CuO QDs. The numbers in the figures represent the particle diameters of CuO QDs.

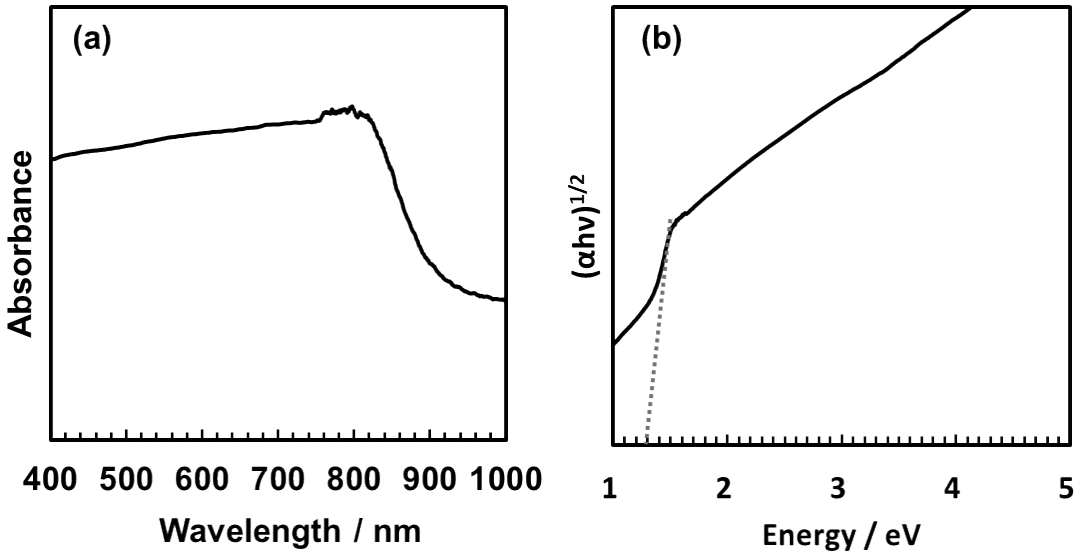

Figure S9 (a) UV-vis spectrum and (b) Tauc plot of bulk CuO.

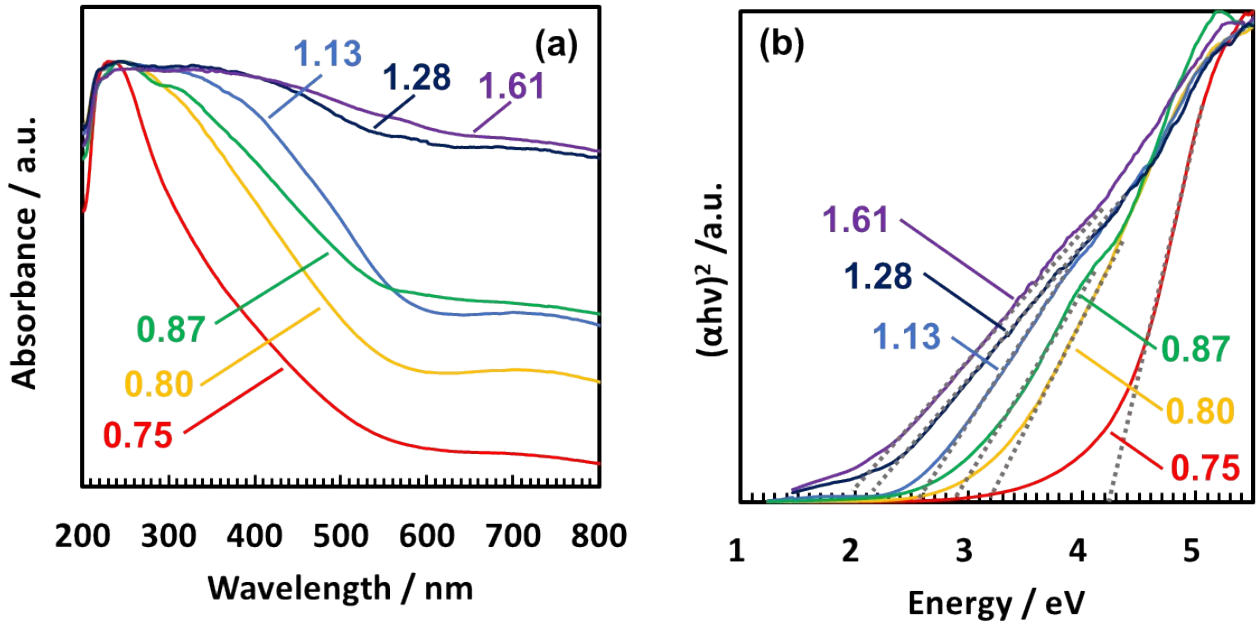

Figure S10 (a) UV-vis spectra and (b) Tauc plots of Cu QDs. The numbers in the figures represent the particle diameters of Cu QDs.

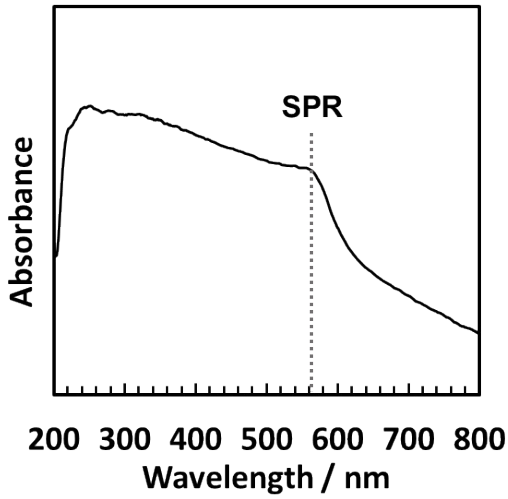

Figure S11 UV-vis spectra of 2.18 nm Cu nanoparticles (SBA15-5M).

Determination of the valence-band edge (E_{vb}) energies of CuO QDs and Cu QDs

The ionization potentials (= valence band–edge energies) of CuO QDs and Cu QDs were determined using photoemission yield spectroscopy in air (PYSA, Riken keiki AC-3).

The threshold photon energy for the photoelectron emission is described as

$$Y \propto (h\nu - \Phi)^n$$

where Y is the photoelectron emission yield, $h\nu$ is the photon energy, and Φ is the threshold energy (ionization potential; work function for metals, valence band–edge energy for semiconductors, highest occupied molecular orbital energy for organic molecules). Empirically, n = 2 was used for the metals and n = 1–3 for the semiconductors.[3] By plotting $Y^{1/n}$ vs $h\nu$, extrapolation of the straight line to intercept to the background level gives the ionization potential. We used n = 3 (semiconductors) for CuO QDs and n = 2 (metals) for Cu QDs.

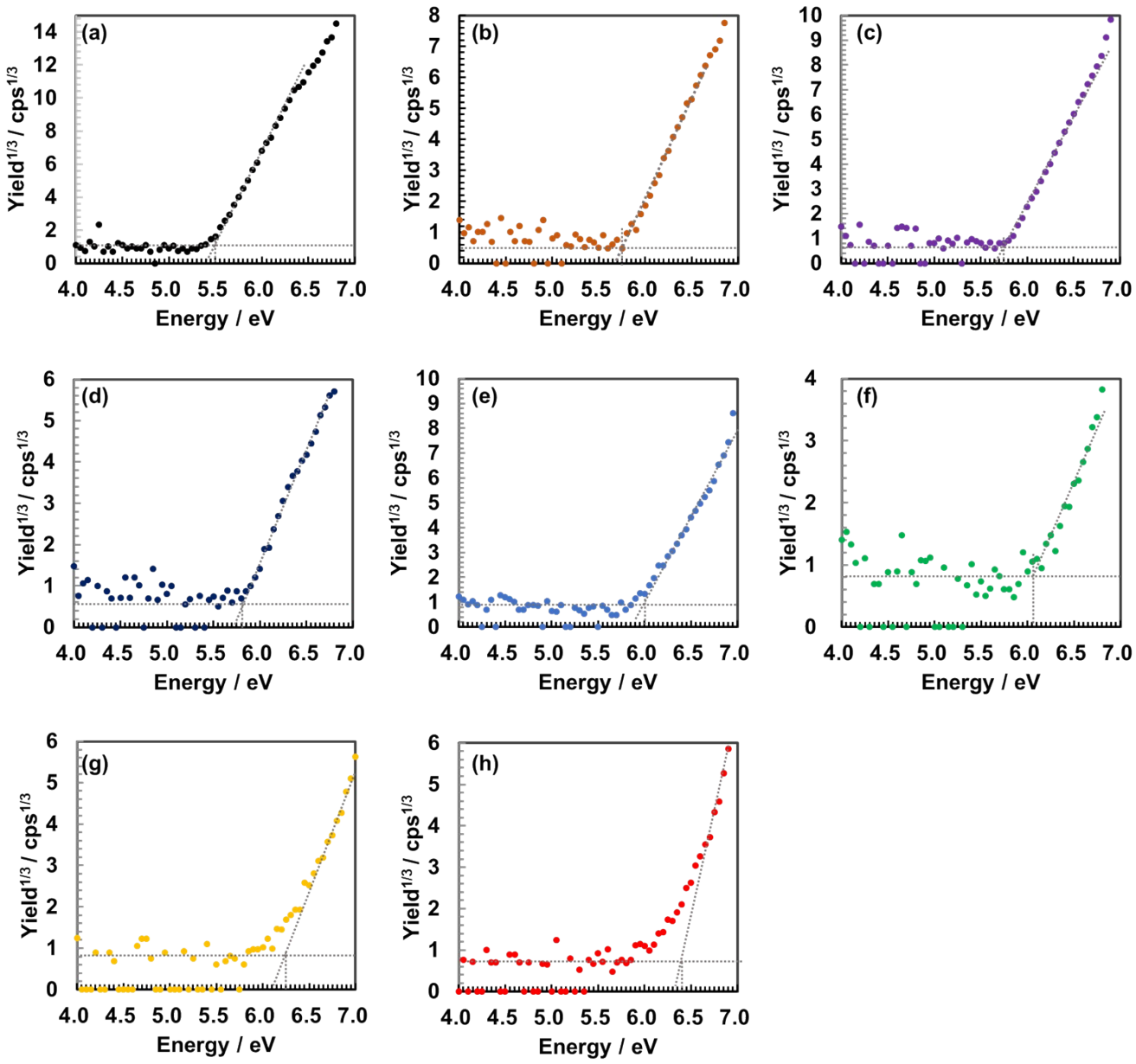

Figure S12 PYSA of CuO QDs. (a) Bulk, (b) SBA15-5M, (c) C18-5M, (d) C18-1M, (e) C18-0.2M, (f) C12-0.2M, (g) C6-0.2M, (h) C6-0.05M.

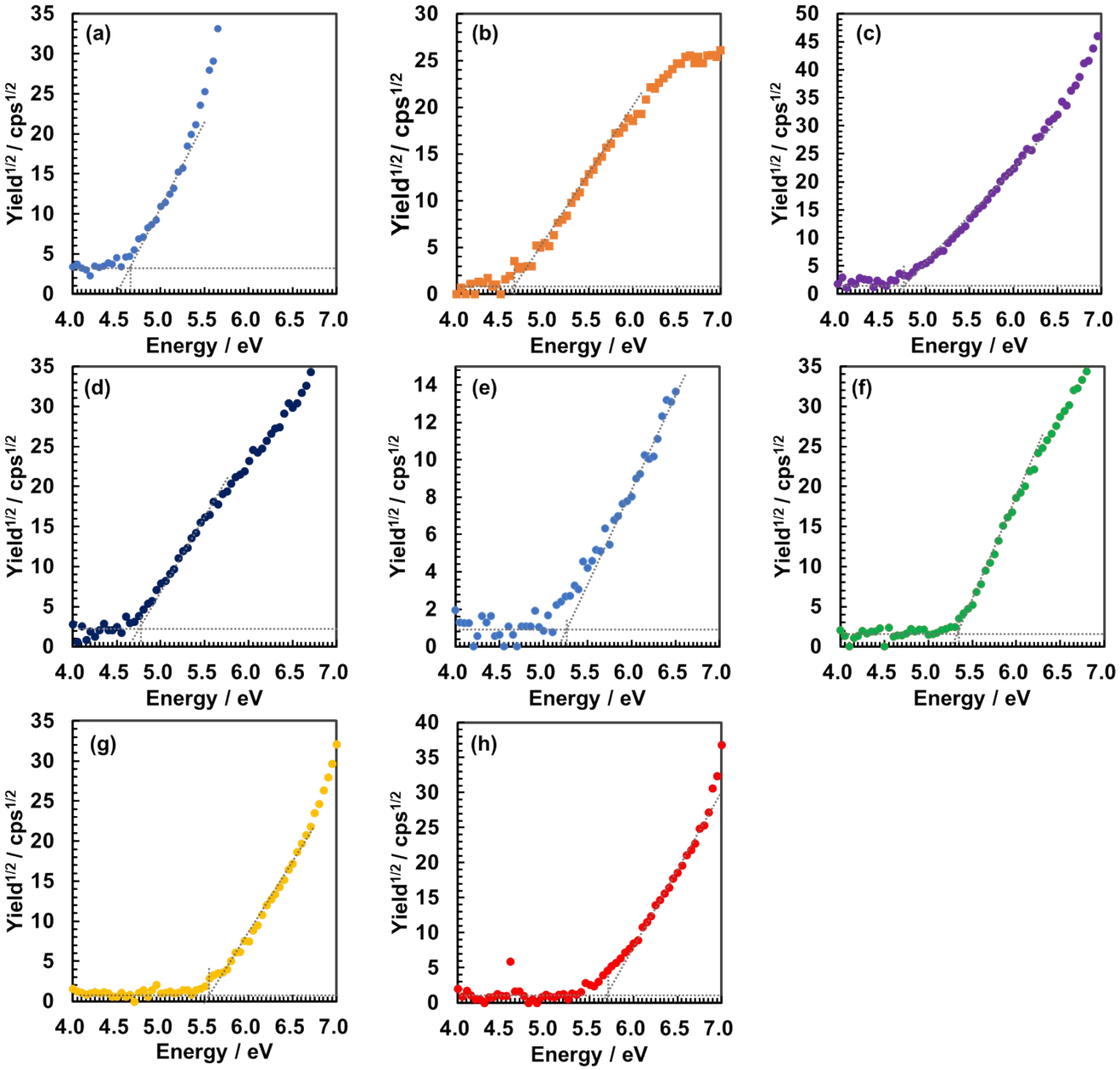

Figure S13 PYSA of Cu QDs. (a) Bulk, (b) SBA15-5M, (c) C18-5M, (d) C18-1M, (e) C18-0.2M, (f) C12-0.2M, (g) C6-0.2M, (h) C6-0.05M.

Table S3 The particle diameter, the bandgap energies, the valence band–edge energies, and the conduction band–edge energies of CuO QDs.

Sample name	Particle diameter (nm)	Bandgap energies (eV)	Valence band edge energies (V_{SHE})	Conduction band edge energies (V_{SHE})
C6-0.05M	0.61	3.22	1.96	-1.26
C6-0.2M	0.71	2.79	1.81	-0.98
C12-0.2M	0.99	2.42	1.61	-0.81
C18-0.2M	1.11	2.31	1.56	-0.75
C18-1M	1.69	1.65	1.36	-0.19
C18-5M	2.10	1.40	1.26	-0.14
Bulk	-	1.35[(a)]	1.06	-0.29

(a) The bandgap energy of bulk CuO was referred from ref. 4a.

Table S4 The particle diameter, the bandgap energies, the valence band–edge energies, and the conduction band–edge energies of Cu QDs.

Sample name	Particle diameter (nm)	Bandgap energies (eV)	Valence band edge energies (V_{SHE})	Conduction band edge energies (V_{SHE})
C6-0.05M	0.75	4.25	1.26	-2.99
C6-0.2M	0.80	3.30	1.11	-2.19
C12-0.2M	0.87	2.90	0.91	-1.99
C18-0.2M	1.13	2.60	0.81	-1.79
C18-1M	1.28	2.13	0.36	-1.77
C18-5M	1.61	1.95	0.26	-1.69

Supplementary Information section 7: Curve fitting with effective mass approximation (EMA) for CuO QDs and Cu QDs.

The relationship between the bandgap energy E_g and the particle radius R of the semiconductor is described by Brus using following equation:

$$E_g = E_{g(bulk)} + \frac{\hbar^2\pi^2}{2R^2}\left(\frac{1}{m_e} + \frac{1}{m_h}\right) - \frac{1.8e^2}{\varepsilon R} + smaller\ terms$$

$$\frac{1}{\mu} = \frac{1}{m_e} + \frac{1}{m_h}$$

E_g : bandgap of QDs (eV)

$E_{g(bulk)}$: bandgap of bulk (eV)

$\hbar$: Dirac's constant = 1.05×10^{-34} (Js)

R : particle radius (m)

μ : reduced mass (kg)

m_e : effective mass of electron (kg)

m_h : effective mass of hole (kg)

m_0 : = 9.11×10^{-19} (C)

ε : permittivity (C^2J^2/m^2)

ε_0 : permittivity = 8.85×10^{-12} (C^2J^2/m^2)

e : elementary charge = 1.60×10^{-19} (C)

1 eV = 1.60×10^{-19} (J)

For CuO QDs, we utilized following values for EMA fitting:

$E_{g(bulk)}$ = 1.35 eV, [4a] m_e = 2.2 m_0,[4c] m_h = 3.25 m_0,[4f] μ = 1.35 m_0, and ε = 18.1ε_0.[4e]

Several different values were reported[4] for CuO, e.g., m_e = 0.65–2.2 m_0, m_h = 1.75–8.4 m_0, and ε = 7.11–18.1ε_0. Using above values, the present experimental data could be fitted well with EMA.

For Cu QDs, we utilized following values for EMA fitting:

$E_{g(bulk)}$ = 1.24 eV, m_e = 1.67 m_0, m_h = 3.69 m_0, and μ = 1.15 m_0.

Since the $E_{g(bulk)}$ is unknown for Cu metal, we used the value that corresponds to the energy difference between the Fermi level and the lowest-lying unoccupied state found in the literature.[5] For the m_e value, we also used a value of this unoccupied state.

The permittivity of the small metal particles was reported to show a size dependency.[6] The values for Cu QDs are still unknown. However, the contribution of the Coulomb term (the 3rd term) is far smaller than that of the quantum localization term (2nd term). Therefore, we exclude the Coulomb term for the EMA of Cu QDs.

The present size dependency of E_g was fitted with various μ values, and we found that by using μ = 1.15 m_0, the EMA curve showed good agreement with the experimental values.

Using m_e = 1.67m_0 and μ = 1.15m_0, m_h was calculated to be 3.69 m_0.

For the EMA fitting of E_{vb} and E_{cb}, we used following equations:

$$E_{vb} = E_{vb(bulk)} + \frac{\hbar^2\pi^2}{2R^2}\left(\frac{1}{m_h}\right)$$

$$E_{cb} = E_{cb(bulk)} + \frac{\hbar^2\pi^2}{2R^2}\left(\frac{1}{m_e}\right)$$

We used experimentally obtained $E_{vb(bulk)}$ (= +1.06 V_{SHE}) and $E_{cb(bulk)}$ (-0.29 V_{SHE}) for CuO. For Cu, we used $E_{vb(bulk)}$ (= +0.24 V_{SHE}) and $E_{cb(bulk)}$ (-1.03 V_{SHE}), which correspond to the experimentally obtained work function of bulk Cu and the lowest unoccupied state found in the literature.[4]

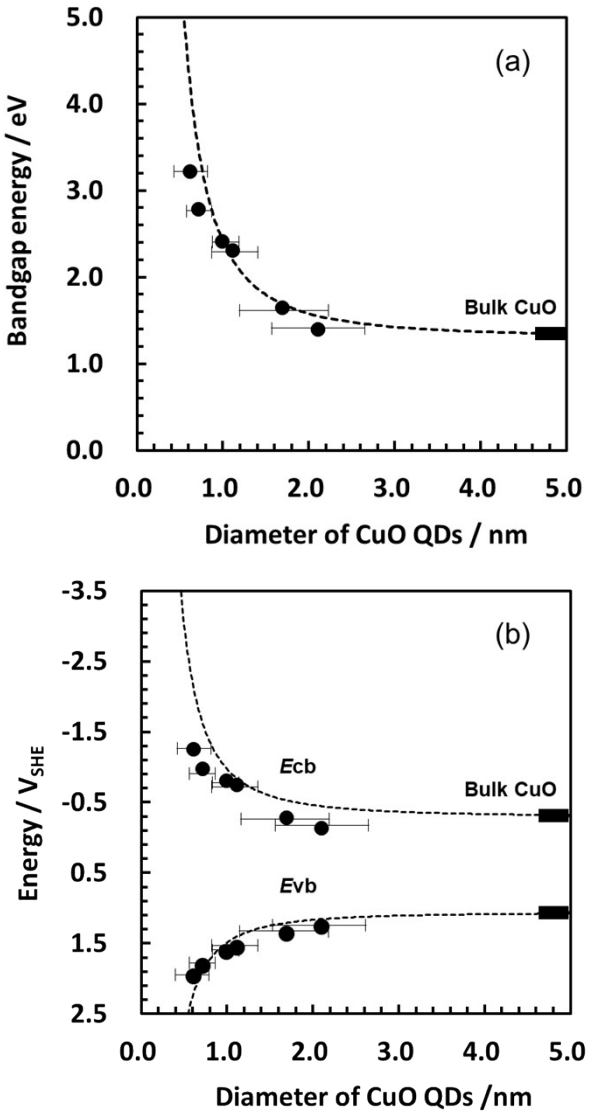

Figure S14 Size dependency of the (a) E_g, (b) E_{vb}, and E_{cb} of CuO QDs. The dotted lines represent curve fitting using the EMA method. The error bars represent the FWHM of particle size distribution profiles shown in Figure S3.

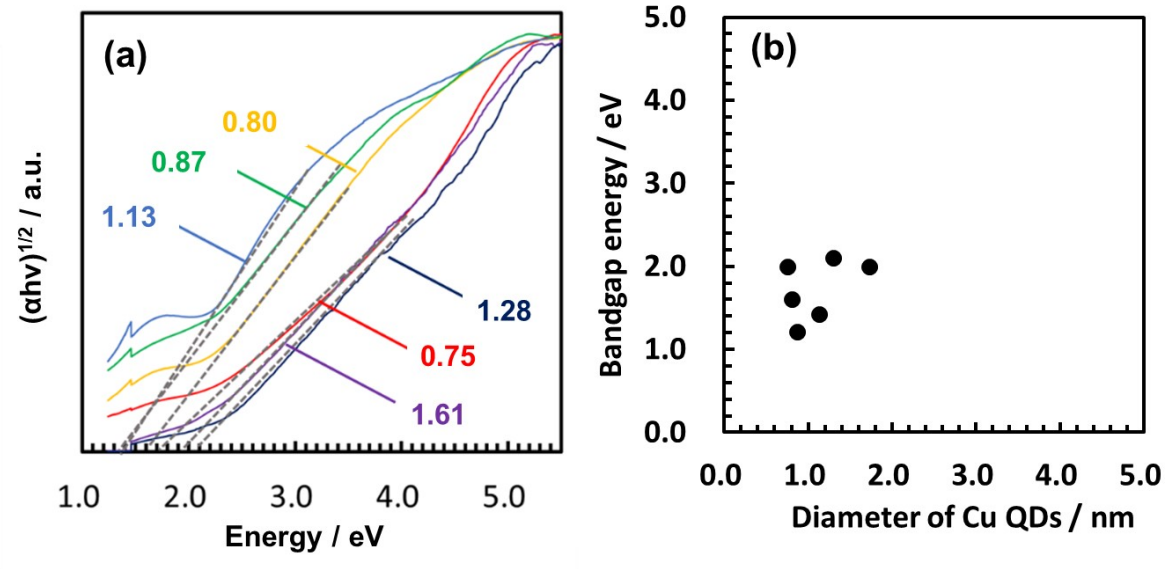

Figure S15 (a) Tauc plots and (b) size dependency of the E_g of Cu QDs from the data analyzed by using the value n = 2 (indirect gap).

References

[1] H. Watanabe, K. Fujikata, Y. Oaki, H. Imai, *Microporous Mesoporous Mater*. 2015, **214**, 41.

[2] a) J. Tauc, *Mater. Res. Bull*. *1970*, **5**, 721; b) B. D. Viezbicke, S. Patel, B. E. Davis, D. P. Birnie III, *Phys. Satus. Solidi. B*, 2015, **252**, 1700.

[3] a) D. Yamashita, Y. Nakajima, A. Ishizaki, M. Uda, *J. Surf. Anal*. 2008, **14**, 433; b) , Jasieniak, M. Califano, S. E. Watkins, *ACS Nano*, 2011, **5**, 5888; c) E. O. Kane, P*hys. Rev.* 1962, **127**, 131.

[4] a) F. P. Koffyberg, F. A. Benko, *Appl. Phys. Lett*. 1982, **53**, 1173; b) Y. Yang, D. X. Qingyong, P. Diao, *Sci. Rep*. 2016, **6**, 35158; c) S. Lany, *J. Phys.: Condens. Matter*, 2015, **27**, 283203; d) Y. S. Tamgadge, G. G. Muley, R. P. Ganorkar, *Opt. Mater*. 2019, **89**, 591; e) N. A. Mohamad, N. Azis, J. Jasni, M. Z. A. A. Kadir, R. Yunus, Z. Yaakub, *Energies*, 2019, **12**, 1605. f) D. Wu, Q. Zhang, M. Tao, *Phys. Rev. B*, 2006, **73**, 235206.

[5] Y. Sonoda, *Phys. Rev. B*, 2011, **83**, 245410.

[6] Z. Jalilian, S. Edalati-Boostan, R. Moradian, *J. Nanophoton*. 2018, **12**, 36004.